

Effects of Ga doping on magnetic and ferroelectric properties of multiferroic delafossite CuCrO 2 : Ab initio and Monte Carlo approaches

Ahmed Al Baalbaky, Yaroslav Kvashnin, Renaud Patte, Raymond Frésard, Denis Ledue

▶ **To cite this version:**

Ahmed Al Baalbaky, Yaroslav Kvashnin, Renaud Patte, Raymond Frésard, Denis Ledue. Effects of Ga doping on magnetic and ferroelectric properties of multiferroic delafossite CuCrO 2 : Ab initio and Monte Carlo approaches. Physical Review B: Condensed Matter and Materials Physics (1998-2015), 2018, 98 (17), pp.174403. 10.1103/PhysRevB.98.174403 . hal-02106756

HAL Id: hal-02106756

https://normandie-univ.hal.science/hal-02106756

Submitted on 23 Apr 2019

HAL is a multi-disciplinary open access archive for the deposit and dissemination of scientific research documents, whether they are published or not. The documents may come from teaching and research institutions in France or abroad, or from public or private research centers.

L'archive ouverte pluridisciplinaire **HAL**, est destinée au dépôt et à la diffusion de documents scientifiques de niveau recherche, publiés ou non, émanant des établissements d'enseignement et de recherche français ou étrangers, des laboratoires publics ou privés.

Effects of Ga doping on magnetic and ferroelectric properties of multiferroic delafossite $CuCrO_2$: *Ab initio* and Monte Carlo approaches

Ahmed Albaalbaky,[1,*] Yaroslav Kvashnin,[2,†] Renaud Patte,[1] Raymond Frésard,[3] and Denis Ledue[1]
[1]*Normandie Université, UNIROUEN, INSA Rouen, CNRS, GPM, 76800 Saint Étienne du Rouvray, France*
[2]*Department of Physics and Astronomy, Division of Materials Theory, Uppsala University, Box 516, SE-75120 Uppsala, Sweden*
[3]*Normandie Université, UNICAEN, ENSICAEN, CNRS, CRISMAT, 14050 Caen, France*

(Received 17 July 2018; revised manuscript received 24 September 2018; published 5 November 2018)

The effects of nonmagnetic impurity doping on magnetic and ferroelectric properties of multiferroic delafossite $CuCrO_2$ are investigated by means of density functional theory calculations and Monte Carlo simulations. Density functional theory calculations show that replacing up to 30% of Cr^{3+} ions by Ga^{3+} ones does not significantly affect the remaining Cr-Cr superexchange interactions. Monte Carlo simulations show that $CuCr_{1-x}Ga_xO_2$ preserves its magnetoelectric properties up to $x \simeq 0.15$ with a spiral ordering, while it becomes disordered at higher fractions. Antiferromagnetic transition shifts towards lower temperatures with increasing x and eventually disappears at $x \geqslant 0.2$. Our simulations show that Ga^{3+} doping increases the Curie-Weiss temperature of $CuCr_{1-x}Ga_xO_2$, which agrees well with experimental observations. Moreover, our results show that the incommensurate ground-state configuration is destabilized by Ga^{3+} doping under zero applied field associated with an increase of frustration. Finally, coupling between noncollinear magnetic ordering and electric field is reported for $x \leqslant 0.15$ through simulating P-E hysteresis loops, which leads to ferroelectricity in the extended inverse Dzyaloshinskii-Moriya model.

DOI: 10.1103/PhysRevB.98.174403

I. INTRODUCTION

Delafossite oxides [1–4] have attracted a lot of attention from researchers due to their interesting novel properties [5] and potential applications. For instance, the simultaneous transparency and p-type conductivity of $CuAlO_2$ [6] and of $PdCoO_2$ in thin-film form [7] may be applied in optoelectronics. Thermoelectric delafossites have been reported, too [8–11]. Furthermore, a strong coupling of the magnetic and structural degrees of freedom paves the way to multiferroics in the magnetic compounds $CuFeO_2$ and $CuCrO_2$ [12–23].

With their layered structure depicted in Fig. 1, ABO_2 delafossites strikingly profile as two-dimensional (2D) materials. This intuition is supported by the electronic transport of $PdCoO_2$, where the anisotropy ratio of the resistivity can reach 1000 at low temperature [24–26]. This strongly suggests the conducting Pd layers should be decoupled from the insulating CoO_2 layers. Yet density functional theory (DFT) calculations yield a quite substantial dispersion of the band crossing the Fermi energy when varying the component of the momentum orthogonal to the layers [27], thereby indicating that the decoupling of the layers is only incomplete [28]. Likewise, for the magnetic compound $CuCrO_2$, recent DFT calculations yielded out-of-plane Heisenberg couplings that are much smaller than the dominant in-plane ones [29].

Delafossite $CuCrO_2$ is a semiconducting compound, with an activation energy close to 280 meV [18]. It crystallizes in the $R\bar{3}m$ space group, with lattice parameters $a = 2.97$ Å and $c = 17.11$ Å [30], forming Cu^+, O^{2-}, and Cr^{3+} triangular layers stacked along the vertical direction, as schematically shown in Fig. 1. The triangular Cr^{3+} ($S = 3/2$) layers are responsible for the magnetism in the compound. $CuCrO_2$ undergoes a magnetic phase transition toward an antiferromagnetic noncollinear state at a Néel temperature $T_N \simeq 24$–27 K [20,29,31,32], with a Curie-Weiss temperature $\theta_{CW} \simeq -(170$–$176)$ K [18,29,31]. In this multiferroic, the magnetic configuration below T_N is a proper-screw spiral incommensurate Y-state known as an ICY state with a magnetic propagation vector $\mathbf{q} = (0.329, 0.329, 0)$ [32]. In this state, the spiral ordering distorts the crystal slightly along the [110] direction [33], leading to the appearance of hard-axis anisotropy along the distorted direction [29]. Such a noncollinear spiral spin structure breaks the space-inversion symmetry leading to the emergence of spontaneous ferroelectricity along the distorted [110] direction through the variation of the hybridization between Cr d orbitals and O p orbitals caused by the spin-orbit coupling [34]. Because, in proper-screw structures, the magnetic propagation vector $\mathbf{q}$ is perpendicular to the spiral plane, magnetoelectric coupling cannot be described by the inverse Dzyaloshinskii-Moriya (DM) model [34–36], but rather by its extended form developed by Kaplan and Mahanti [37]. Thus, ferroelectric polarization induced between two canted spins $\mathbf{S}_i$ and $\mathbf{S}_j$ is given by

$$\mathbf{P}_{ij} \propto \mathbf{e}_{ij} \times (\mathbf{S}_i \times \mathbf{S}_j) + (\mathbf{S}_i \times \mathbf{S}_j), \tag{1}$$

where $\mathbf{e}_{ij}$ is a unit vector joining sites i and j. On the other hand, it was shown that doping $CuCrO_2$ with nonmagnetic ($S = 0$) impurities allows exploring novel phenomena in such a quasi-2D compound [38]. For example, it was found that

*ahmed.baalbaky@hotmail.com
†yaroslav.kvashnin@physics.uu.se

 ©2018 American Physical Society

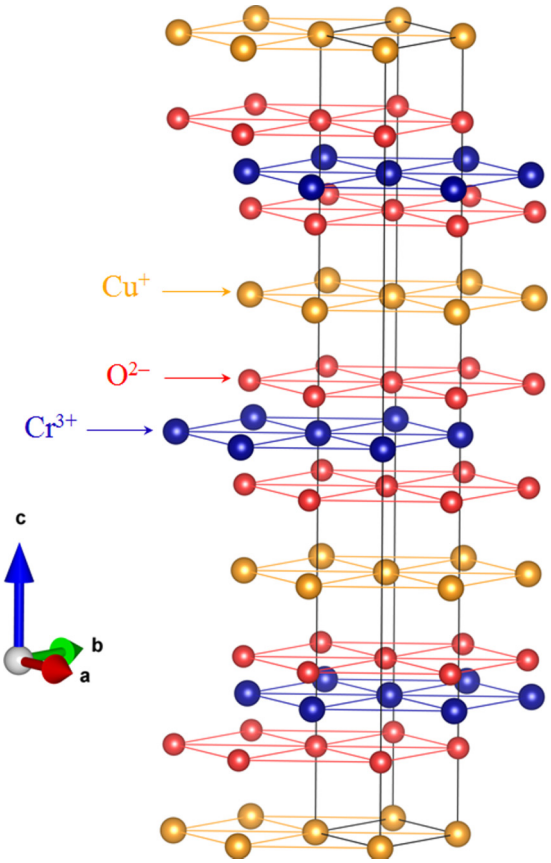


FIG. 1. Crystal structure of delafossite ABO_2 (A=Cu, B=Cr) with the hexagonal unit cell.

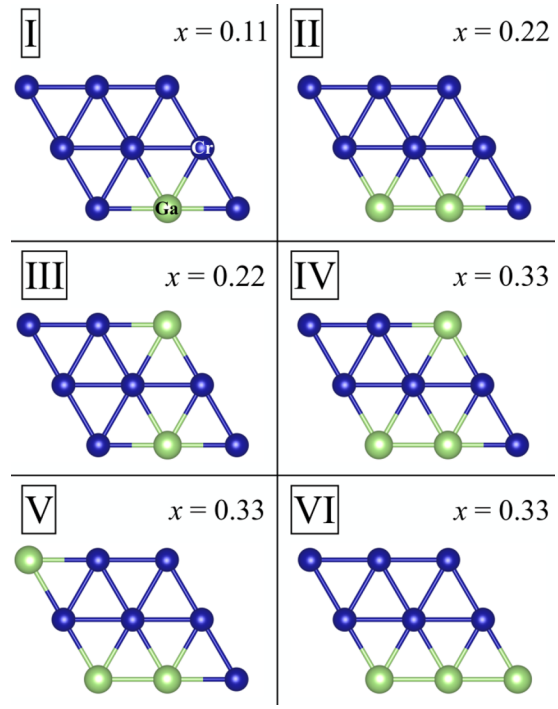


FIG. 2. Modeled structural configurations. Cr (Ga) atoms are represented by blue (green) spheres. Cu and O atoms are omitted. Configuration I corresponds to $x \approx 0.11$; II and III correspond to $x \approx 0.22$, and IV, V, and VI correspond to $x \approx 0.33$.

spiral ordering under zero applied magnetic field can be destabilized by the substitution of Cr^{3+} by Al^{3+} [39,40]. However, an increase in T_N was seen by the substitution of Cr^{3+} by Mg^{2+} [41,42], reflecting the important role of hole doping in the phase transition. It was also shown that doping $CuCrO_2$ by Ga^{3+} in the Cr^{3+} sites results in a material that may combine the good characteristics from both semiconductors $CuCrO_2$ and $CuGaO_2$ [43,44]. This case of Ga^{3+} doping is very crucial because it allows studying the effect of magnetic dilution in $CuCr_{1-x}Ga_xO_2$ without a steric effect [45] due to the very close ionic radii of Cr^{3+} ($r_{Cr^{3+}} = 61.5$ pm) and Ga^{3+} ($r_{Ga^{3+}} = 62$ pm). Indeed, no significant change in the structural parameters of the unit cell of $CuCrO_2$ has been detected [45]. On the other hand, it was shown that Ga^{3+} directly affects the antiferromagnetic nature of the compound, leading to the possibility of a spin glass behavior [46]. Moreover, neutron powder diffraction experiments performed on $CuCr_{0.9}Ga_{0.1}O_2$ showed that the magnetic peaks observed at 1.8 K correspond to a propagation vector $\mathbf{q} = (0.329, 0.329, 0)$ where they are significantly broadened compared to that of $CuCrO_2$, which evidences a disorder in the magnetic configuration [45]. Nevertheless, magnetoelectric properties of $CuCr_{1-x}Ga_xO_2$ are still rarely studied, and therefore, complementary investigations are necessary for better understanding of these materials. Based on that, we aim to investigate the effects of Ga^{3+} doping on the magnetic and ferroelectric properties of multiferroic $CuCrO_2$ by means of DFT calculations and Monte Carlo (MC) simulations.

The remainder of this paper is organized as follows: Sec. II presents the DFT computational details. Section III presents the model and MC method. Section IV is devoted to discussions of the obtained results, and a conclusion is given in Sec. V.

II. DFT COMPUTATIONAL DETAILS

Conventional DFT calculations usually underestimate the value of the band gap (or even predict metallic solution) for transition-metal oxides. The DFT+U [47] method has been shown to improve the situation for pristine $CuCrO_2$, providing optical gaps and valence band spectra in good agreement with experiments [5,18,48]. For this study we apply the Hubbard correction to Cr 3d states by setting Hubbard U and Hund's J_H parameters to 2.3 and 0.9 eV, respectively, following previous studies for undoped $CuCrO_2$ [19,29].

DFT+U calculations are performed using the full-potential linear muffin-tin orbital method as implemented in the RSPT [49] software. In order to model Ga doping, a $3 \times 3 \times 1$ supercell of $CuCrO_2$ is constructed. Substituting one, two, or three Cr atoms for Ga allows us to model the following concentrations: $x \approx 0.11$, 0.22, and 0.33. For a given concentration, we simulate several different atomic arrangements. In total, we consider six different atomic arrangements, which are depicted in Fig. 2.

All other computational details are exactly the same as the ones used in our previous work on pristine $CuCrO_2$ [29]. For that study, the calculations were performed for a ferromagnetic state, and a good description of the magnetic properties was achieved. Here we follow the same recipe in order not to

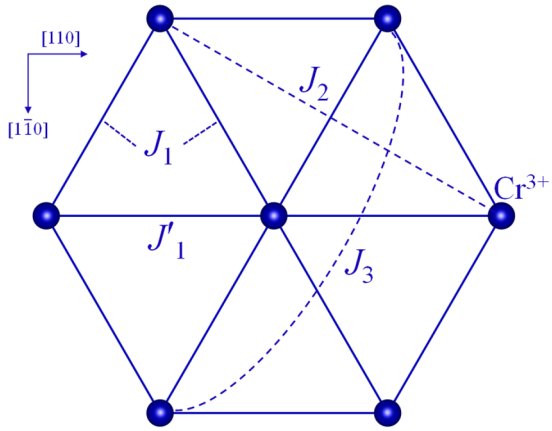


FIG. 3. Schematic representation of the considered intralayer exchange paths between Cr^{3+} ions.

complicate the DFT calculations with spin noncollinearity. In order to quantify the effect of lattice relaxation introduced by Ga doping, optimization of the atomic positions is performed for $x \approx 0.11$ using VASP [50,51]. Since DFT equilibrium lattice constants are off from experiment by a few percent, it is common to discuss the *relative* structural modifications with respect to the pristine system. According to our results, the differences between nearest-neighbor Ga-O and Cr-O bond distances is less than 0.1%; thus, the effects of lattice distortions can safely be neglected. In order to be consistent with the previous study, all the results presented in this work are obtained for an unrelaxed $CuCrO_2$ structure. Heisenberg exchange parameters are calculated using the magnetic force theorem [52,53] as implemented in the RSPT [54] code.

III. MODEL AND MONTE CARLO METHOD

A model based on triangular lattices stacked vertically along the c axis is used to build a three-dimensional (3D) simulation box ($L \times L \times L_z$). The single unit cell of $CuCrO_2$ contains three Cr^{3+} ions located at $(a/3, 2a/3, c/6)$, $(0, 0, c/2)$, and $(2a/3, a/3, 5c/6)$. The hexagonal symmetry of $CuCrO_2$ results in a complex network with several intra- and interlayer superexchange paths. Within our model, we consider three intralayer interactions (J_1, J'_1, J_2, and J_3, shown in Fig. 3) and an interlayer interaction (J_4). Note that $S = 3/2$ is large enough to treat classically; therefore, 3D vectors are considered to model Cr^{3+} spins, and the classical Heisenberg Hamiltonian is used to model exchange interactions. Our total Hamiltonian is then given by

$$H = -\sum_{\langle i,j\rangle} J_{ij}\mathbf{S}_i \cdot \mathbf{S}_j - D_x \sum_i S_{ix}^2 - D_z \sum_i S_{iz}^2 + g\mu_B \mathbf{B} \cdot \sum_i \mathbf{S}_i - A_0 \mathbf{E} \cdot \sum_{\langle i,j\rangle} \mathbf{S}_i \times \mathbf{S}_j, \quad (2)$$

where J_{ij} stands for exchange interactions between interacting spins $\mathbf{S}_i$ and $\mathbf{S}_j$, the x axis corresponds to the [110] direction, and the z axis corresponds to the [001] direction. $D_x < 0$ and $D_z > 0$ refer to the hard- and easy-axis anisotropy constants, respectively. The fourth term corresponds to the Zeeman energy, where $\mathbf{B}$ is an applied magnetic field (μ_B is the Bohr magneton, and $g = 2$ is the Landé factor). The last term of the Hamiltonian represents the coupling between the spins and an applied electric field $\mathbf{E}$ where the sum runs over the magnetic bonds along the [110] direction. A_0 is a coupling constant related to the spin-orbit and spin-exchange interactions [20]. The latter contribution evidences the direct coupling between ferroelectricity and magnetic ordering in proper-screw structures ($\mathbf{P}_{ij} \propto \mathbf{S}_i \times \mathbf{S}_j$) and allows modeling ferroelectric properties as proposed by Kaplan and Mahanti [37].

Since Ga^{3+} is nonmagnetic and produces neither steric effects nor additional holes upon doping in the Cr^{3+} sites, we treat the impurity as a lattice vacancy where we discard all the surrounding interactions as well as the single-ion anisotropy at the substituted site.

To characterize the magnetic ordering relative to the ICY state, we calculate the vector chirality per plane, defined as

$$\boldsymbol{\kappa} = \frac{1}{N_m}\frac{1}{S^2}\frac{2}{3\sqrt{3}}\sum_p (\mathbf{S}_1 \times \mathbf{S}_2 + \mathbf{S}_2 \times \mathbf{S}_3 + \mathbf{S}_3 \times \mathbf{S}_1), \quad (3)$$

where N_m is the number of magnetic bonds in each triangular plane and the sum runs over the triangular plaquettes in each plane. After that we calculate

$$\Gamma = \frac{1}{N_{\text{planes}}}\sum_{\text{planes}} |\boldsymbol{\kappa}|, \quad (4)$$

the average of the norm of $\boldsymbol{\kappa}$ over the number of planes N_{planes} in the system. In the ICY state, $\Gamma \approx 1$, and the spins lie in the (110) spiral plane if $\boldsymbol{\kappa}$ is along the [110] direction, while $\Gamma < 1$ reflects the destabilization of the ICY state. The energy of the ICY state in the distorted infinite crystal is calculated as

$$E_{\text{ICY}}(q) = -S^2(1-x)[J'_1\cos(4\pi q) + 2J_1\cos(2\pi q) + J_2 + 2J_2\cos(6\pi q) + J_3\cos(8\pi q) + 2J_3\cos(4\pi q) + J_4 + 2J_4\cos(2\pi q)], \quad (5)$$

where x represents the fraction of Ga^{3+} ions in the system and q is the propagation vector corresponding to a given set of exchange interactions. The simulated ground-state (GS) energy will be compared to E_{ICY} to characterize the stable magnetic configuration relative to the ICY state for $x \neq 0$.

MC simulations [55] are performed on $46 \times 46 \times 2$ (six atomic planes) stacked triangular lattices with periodic boundary conditions using the standard Metropolis algorithm [56]. Hysteresis loops are simulated using the time step quantified algorithm [57] with the Metropolis transition probability. At each temperature, 10^5 MC steps are performed for thermal averaging after discarding 5×10^3 MC steps for thermal equilibration. Various Ga^{3+} fractions ($x =$ 0, 0.02, 0.05, 0.1, 0.15, 0.2, and 0.3) are considered. For each fraction, random substitution of $S = 0$ sites takes place through the whole system. Thus, the configurational average over randomness is necessary to obtain the correct bulk properties. Here the configurational average is done over 112 different doped configurations with different random-number sequences.

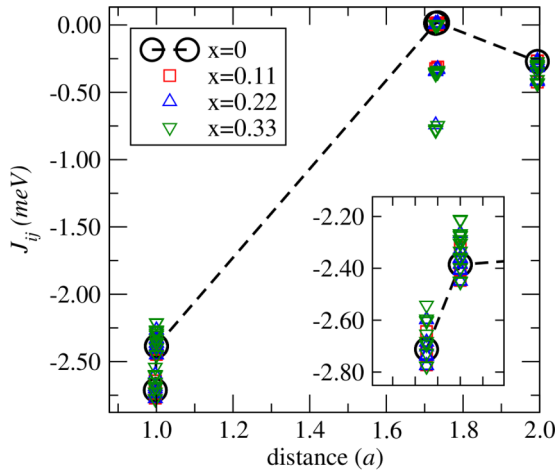


FIG. 4. Calculated Cr-Cr exchange interactions in $CuCr_{1-x}Ga_xO_2$ as a function of the distance (in units of the lattice constant) for different values of x. Inset: Zoomed-in image showing only J_1 and J_1' interactions.

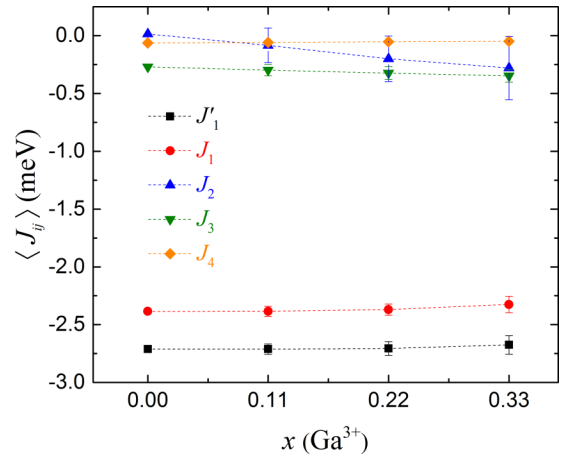


FIG. 5. Calculated averaged Cr-Cr exchange interactions in $CuCr_{1-x}Ga_xO_2$ for different concentrations x. The bars on the symbols denote the standard deviation from the mean value of each J_{ij}.

IV. RESULTS AND DISCUSSION

A. Main outcomes of DFT calculations

Our calculations predict the undoped system is insulating with a fundamental gap of about 1.52 eV. The obtained value is in good agreement with the experimental estimate of 1.28 eV [58]. Upon Ga doping, the fundamental gap tends to slightly increase, reaching a value of 1.6 eV for the highest studied concentration ($x \approx 0.33$). For all considered structural configurations (Fig. 2), the magnetic moments of Cr ions are close (within $0.02\mu_B$ uncertainty) to the value obtained for the undoped system, which is about $2.62\mu_B$. The calculated exchange interactions for various Ga concentrations for all superexchange paths are shown in Fig. 4. The results obtained for all considered structural models and all Cr atoms in the $3 \times 3 \times 1$ supercells are shown together.

In order to clearly see the trends in the different exchange interactions, we compute the averaged exchange couplings over the different individual bonds as well as the various configurations corresponding to a given concentration with their corresponding standard deviations using the data shown in Fig. 4. The results are given in Fig. 5. For the configuration with $x \approx 0.11$, it can be seen that the estimates of the various exchange interactions are roughly the same as for $x = 0$. For larger x, among all considered couplings, the J_2 coupling is the most affected by Ga doping, showing the largest standard deviations and the most pronounced shift of its mean value.

The reason for this can be inferred by examining the projected density of states (DOS). In Fig. 6(a) we show the calculated total and partial DOSs for configuration II (Fig. 2), corresponding to a Ga concentration of $x \approx 0.22$. As one can see, the s and p states of Ga hybridize with the p states of the neighboring oxygen sites. This means that Ga orbitals are able to affect the superexchange between the distant Cr atoms by providing an additional contribution from the Cr-O-Ga-O-Cr exchange paths. This is further supported by Fig. 6(b), where the real-space picture of the J_2 couplings for one of the Cr atoms is presented. An inspection of Fig. 6(b) reveals that the more Ga atoms there are in the proximity of the corresponding Cr-Cr bond, the larger the change in J_{ij} is with respect to the undoped case [$J_2(x = 0) \approx 0.012$ meV].

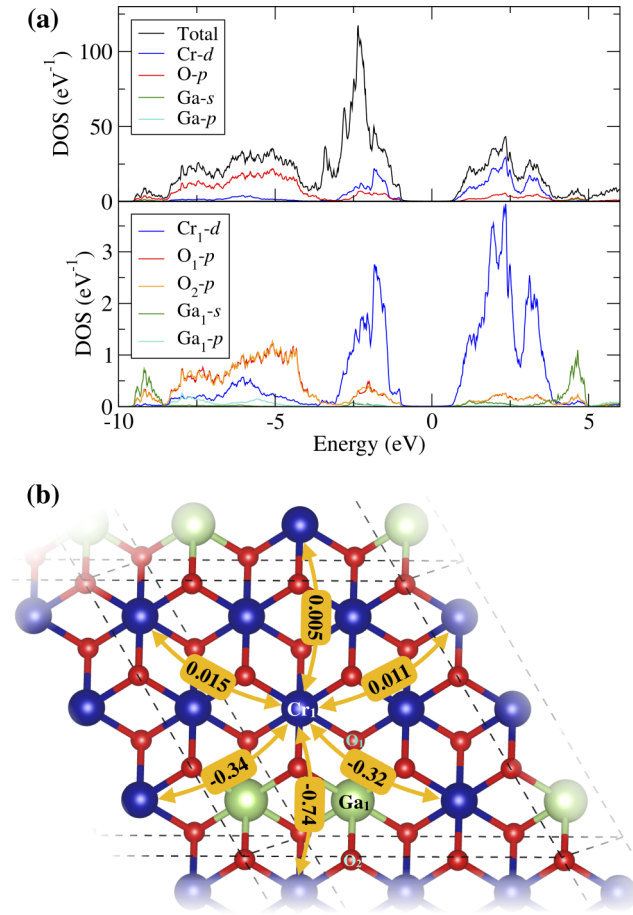


FIG. 6. (a) Total and partial densities of states calculated for configuration II in Fig. 2 and (b) the next-nearest-neighbor exchange couplings J_2 (in meV) for the Cr_1 atom in the same structural configuration.

Nevertheless, the dominant exchange couplings J_1 and J_1' are quite robust and show no significant effect on Ga impurities because they have shorter exchange paths, i.e., Cr-O-Cr, which are not mediated by Ga atoms and hence do not depend on their distribution.

Note that it is not correct to interpret the results shown in Fig. 5 as an induced *disorder* in the exchange couplings as is typically done because the modifications of the couplings are not random but appear strictly in the proximity of the Ga sites. The facts that these modifications are small for the dominant interactions and that J_2 does not play an essential role in magnetic ordering (due to its smallness relative to J_1 and J_1') allow us to neglect these effects. Hence, for our further MC simulations we use the original set of Cr-Cr exchange interactions corresponding to the undoped $CuCrO_2$ [29] for all Ga concentrations.

B. Ground state and phase transition

In this part, we study the effect of Ga^{3+} doping on the GS configuration of $CuCrO_2$ as well as phase transition. We start our simulations from random spin configurations at a high enough temperature ($T_i = 35.01$ K) above the transition temperature of the pure system. We then slowly cool the system down to a final temperature $T_f = 0.01$ K according to $T_{i+1} = T_i - \Delta T$, with $\Delta T = 0.5$ K. In $CuCrO_2$ ($x = 0$), the simulated value of the propagation vector $\mathbf{q} = (0.326, 0.326, 0)$ is very close to $\mathbf{q} = (0.329, 0.329, 0)$ reported experimentally [32], evidencing that the simulated GS configuration is the ICY state. In addition, we find $\Gamma = 0.998$ at T_f, in excellent agreement with its theoretical value calculated for $q = 0.326$ according to

$$\Gamma_{\text{theo}} = \frac{2}{3\sqrt{3}}[2\sin(2\pi q) - \sin(4\pi q)] = 0.998. \quad (6)$$

For preliminary information about the GS when $x \neq 0$, we compare the simulated GS exchange energy per spin E_{GS} with that calculated for the ICY state according to Eq. (5). The dependence of E_{GS} and E_{ICY} on x in $CuCr_{1-x}Ga_xO_2$ is plotted in Fig. 7. It can be seen that E_{GS} increases linearly with x due to the loss of magnetic interactions caused by the introduced vacancies. In comparison with the energy of the ICY state, it can be noticed that E_{GS} is below E_{ICY} for $x \neq 0$. This means that the ICY state is no longer stable in $CuCr_{1-x}Ga_xO_2$. In addition, $\Gamma < 1$ and decreases when $x \neq 0$, confirming the destabilization of the ICY state in $CuCr_{1-x}Ga_xO_2$ (Fig. 8). Moreover, we find that $\boldsymbol{\kappa}$ is along the [110] direction for $x \leqslant 0.2$, suggesting that the (110) plane remains a spiral plane in these diluted antiferromagnets. The latter is confirmed by calculating the average of the absolute value of the spin components according to

$$\sigma_u = \frac{1}{N}\left\langle \sum_i |S_u^i| \right\rangle_T, \quad (7)$$

where N is the number of spins, $u = x, y, z$, and $\langle \cdots \rangle_T$ means thermal averaging. Figure 8 shows that $\sigma_x \simeq 0$ for $x \leqslant 0.2$, confirming that the spins lie in the (110) plane, whereas $\sigma_x \neq 0$ for $x = 0.3$, indicating that the spins go out of the (110) plane.

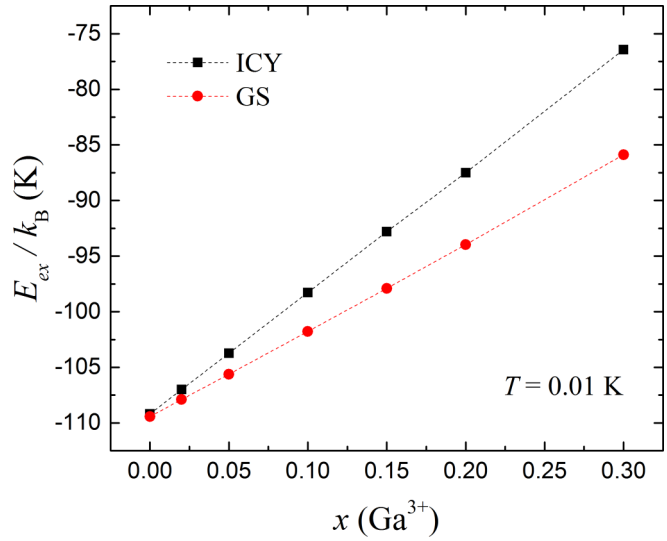


FIG. 7. Variation of the simulated GS exchange energy per spin compared to E_{ICY} calculated for $q = 0.326$ as functions of x in $CuCr_{1-x}Ga_xO_2$.

To localize T^*, the temperature when spiral ordering emerges, we calculate the chiral susceptibility according to [59]

$$\chi_\Gamma = \langle \Gamma^2 \rangle_T - \langle \Gamma \rangle_T^2. \quad (8)$$

Figure 9 shows the thermal variation of χ_Γ simulated for $x \leqslant 0.2$. It can be seen that T^* decreases with increasing x. For $x = 0$, $T^* = 28.5 \pm 0.5$ K, which corresponds to the Néel temperature of $CuCrO_2$ [29]. However, upon doping, it is important to check whether spiral ordering still coexists with a phase transition or phase transition takes place at another stage or no longer exists.

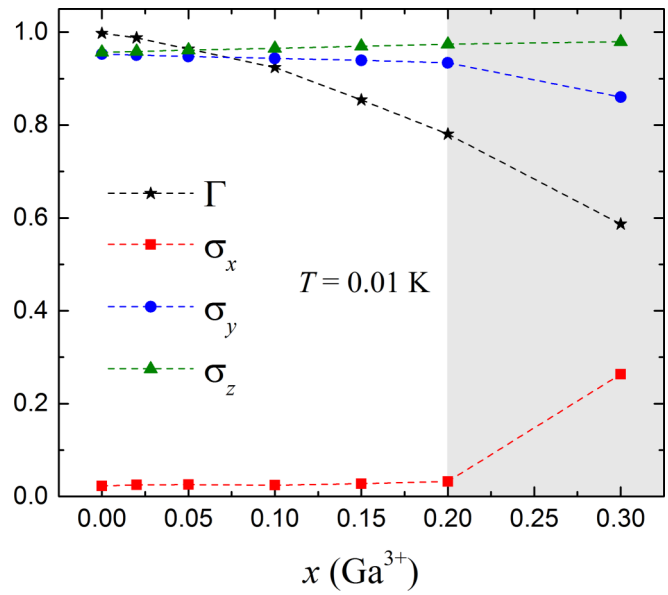


FIG. 8. Variation of Γ, σ_x, σ_y, and σ_z as functions of x in $CuCr_{1-x}Ga_xO_2$.

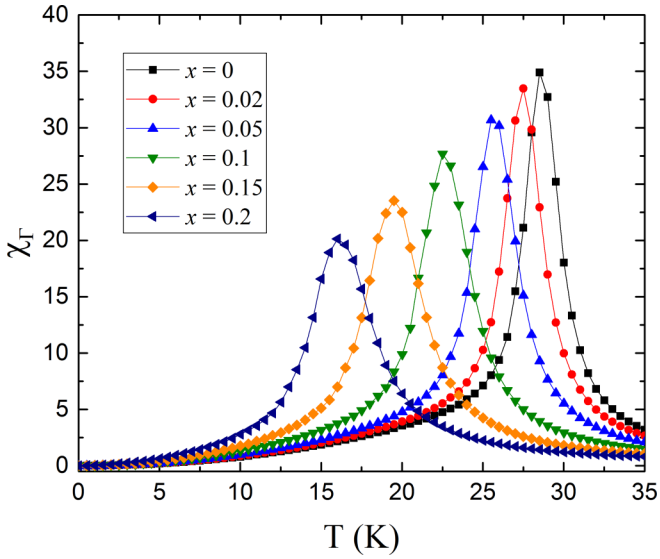


FIG. 9. Simulated temperature dependence of χ_Γ in $CuCr_{1-x}Ga_xO_2$.

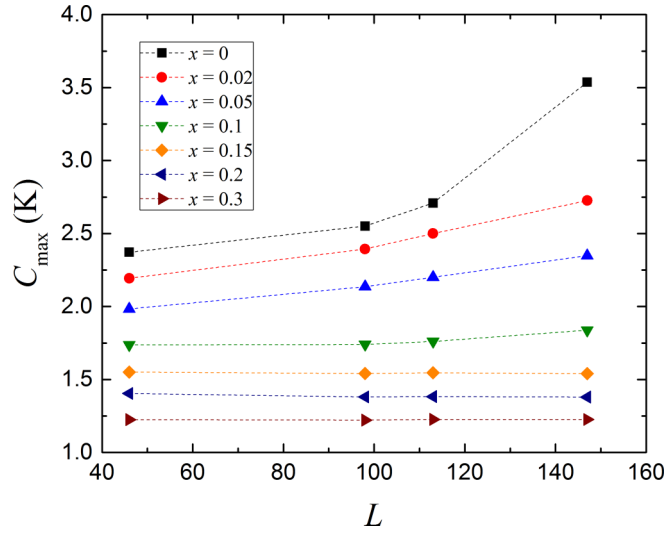


FIG. 11. Simulated size dependence of the specific heat maximum in $CuCr_{1-x}Ga_xO_2$ (error bars are smaller than symbols).

To answer the latter point, we calculate the specific heat per spin according to

$$C = \frac{1}{N}\frac{\partial U}{\partial T} = \frac{\langle E^2\rangle_T - \langle E\rangle_T^2}{Nk_BT^2}, \tag{9}$$

where $U(T) = \langle E\rangle_T$, with E being the energy of each magnetic configuration given by Eq. (2), and k_B is the Boltzmann constant. Figure 10 shows the temperature profile of C simulated for each fraction of Ga^{3+}. It can be seen that the specific heat peak is rounded and shifts towards lower temperatures with increasing x. Starting from $x = 0.2$, the specific heat peak is broadened, and thus, no precise T_{peak} can be identified. Precise information about the phase transition can be gained by investigating size effects on C_{max}. Up to $L = 147$, it can be noticed that C_{max} increases with L for $x \leqslant 0.1$ (Fig. 11), indicating a second-order phase transition and long-range ordering in these compounds. Thus, we can say that the T_{peak} here corresponds to T_N. For $x > 0.1$, C_{max} does not respond to size variation; this may result from the loss in long-range ordering due to the introduced vacancies and/or a change in the nature of the transition. To validate the latter predictions, we calculate the spin-spin correlation functions along the [100] direction according to $G(R, T) = \langle \mathbf{S}_i \cdot \mathbf{S}_j\rangle_T/S^2$, with R being the separation distance between the pairs $\mathbf{S}_i, \mathbf{S}_j$. Figure 12 shows the variation of $G(R, T)$ as a function of R simulated near T_{peak}. It can be clearly seen that antiferromagnetic long-range ordering persists for $x \leqslant 0.15$, while it starts to disappear for $x = 0.2$ and is suddenly lost at $x = 0.3$. The latter confirms the broadening of C_{peak} seen for $x \geqslant 0.2$ in Fig. 10. Therefore, disordered states are expected for $x \geqslant 0.2$, while antiferromagnetic ordered states still exist when $x \leqslant 0.15$, and their transition and spiral ordering temperatures are listed in Table I. At these fractions, we can see that spiral ordering emerges simultaneously with the antiferromagnetic transition. This classifies $CuCr_{1-x}Ga_xO_2$ as a magnetic multiferroic [60] and makes it very interesting since ferroelectricity emerges in the magnetically ordered state. To validate our estimates of phase transition temperatures and to confirm the magnetic nature of each composition of $CuCr_{1-x}Ga_xO_2$, magnetic measurements under a small applied magnetic field are necessary.

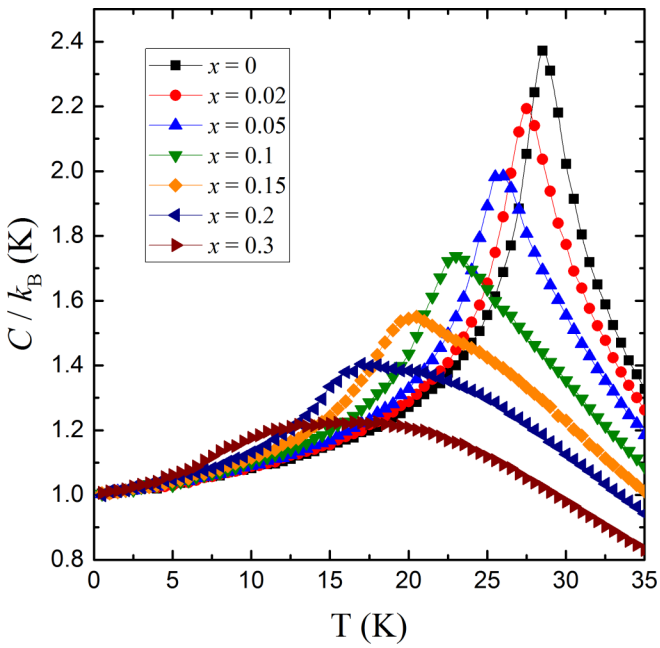


FIG. 10. Simulated temperature dependence of the specific heat per spin in $CuCr_{1-x}Ga_xO_2$.

TABLE I. Estimated transition temperatures extracted for $L = 147$ in $CuCr_{1-x}Ga_xO_2$ ($x \leqslant 0.15$).

x	0	0.02	0.05	0.1	0.15
$T_N \pm 0.5$ (K)	28.0	26.5	25.0	21.5	18.0
$T^* \pm 0.5$ (K)	28.0	26.5	25.0	21.5	18.0

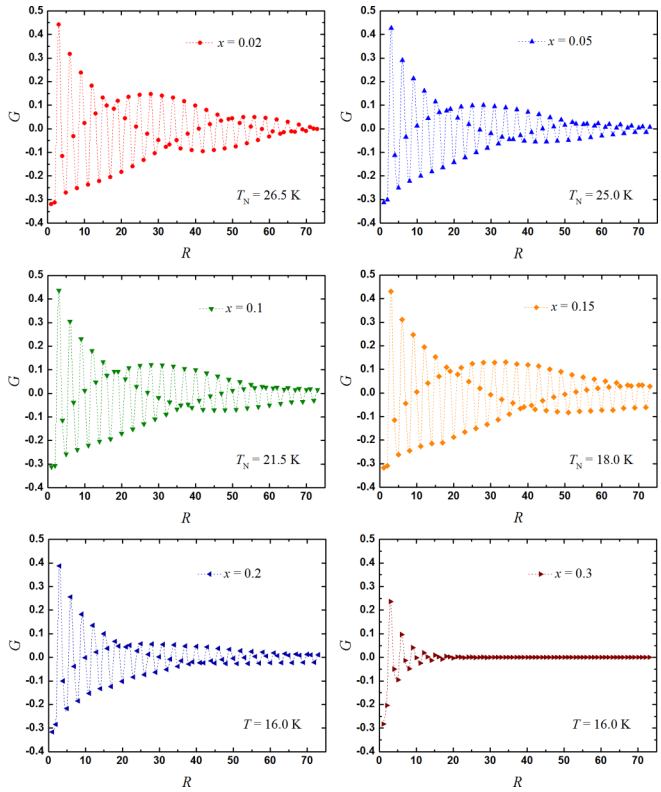


FIG. 12. Variation of the simulated normalized spin-spin correlations along the [100] direction near the transition for $L = 147$ in $CuCr_{1-x}Ga_xO_2$.

C. Magnetic properties under a small applied magnetic field

Magnetic properties under a 0.3 T magnetic field applied along the [110] direction are simulated between 300 and 6 K to calculate the magnetization per μ_B per spin, defined as

$$M_B = -\frac{g}{N}\,\mathbf{e}_B \cdot \sum_i \mathbf{S}_i, \tag{10}$$

with $\mathbf{e}_B$ being a unit vector along the magnetic field direction. From these magnetization measurements, one can gain further information about magnetic interactions as well as magnetic frustration in the system by estimating the Curie-Weiss temperature θ_{CW}.

We start each simulation from a random spin configuration at $T_i = 300$ K, and we then cool the system down to $T_f = 6$ K with a constant temperature step $\Delta T = 2$ K. The simulated temperature dependence of M_B per spin for each fraction x is plotted in Fig. 13. It can be seen that the high-temperature region of M_B, for all fractions, obeys well the Curie-Weiss law $M_B/H = \mathscr{C}/(T - \theta_{CW})$, with $\mathscr{C}$ being the Curie constant. A small increase in M_B can be seen as x increases. This is because the molecular field due to the interactions with the various sublattices acts against the magnetization at high temperatures. As x increases, the magnitude of the molecular field decreases due to the loss in magnetic bonds inducing the small increase in M_B. Such an increase in M_B leads to a decrease in $|\theta_{CW}|$, as shown in Fig. 14, which displays very good agreement with the experimental observations [45]. It is worth noting that for $x = 0.3$, the M_B behavior is still far from

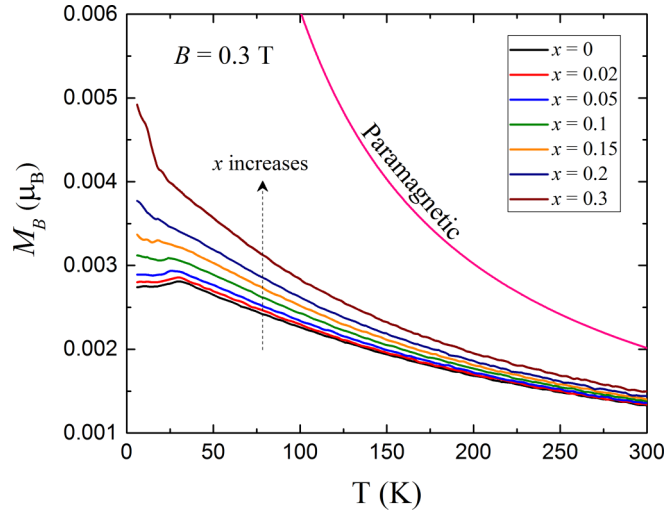


FIG. 13. Simulated temperature dependence of the magnetization per spin under $B = 0.3$ T in $CuCr_{1-x}Ga_xO_2$.

that of the ideal paramagnet (Fig. 13), indicating that even in the disordered state seen in $CuCr_{0.7}Ga_{0.3}O_2$, local interactions have non-negligible effects ($\theta_{CW} \neq 0$).

On the other hand, the low-temperature part depends on x, and we can see different behaviors. For $x \leqslant 0.1$, the magnetization curves possess cusps consistent with the peaks seen at the specific heat curves, as shown in Fig. 15. Below these cusps, M_B slightly decreases with temperature, suggesting that $CuCr_{1-x}Ga_xO_2$ still undergoes a phase transition toward an antiferromagnetic state which is in agreement with the presence of antiferromagnetic long-range ordering at these fractions (Fig. 12). A change in behavior starts in the vicinity of $x = 0.15$, where we can still see a cusp in the low-temperature part (which is more affected by statistical fluctuations), which may indicate an antiferromagnetic transition. Our observations are consistent with the experimental results [45] in terms of the decrease of T_N as x increases with-

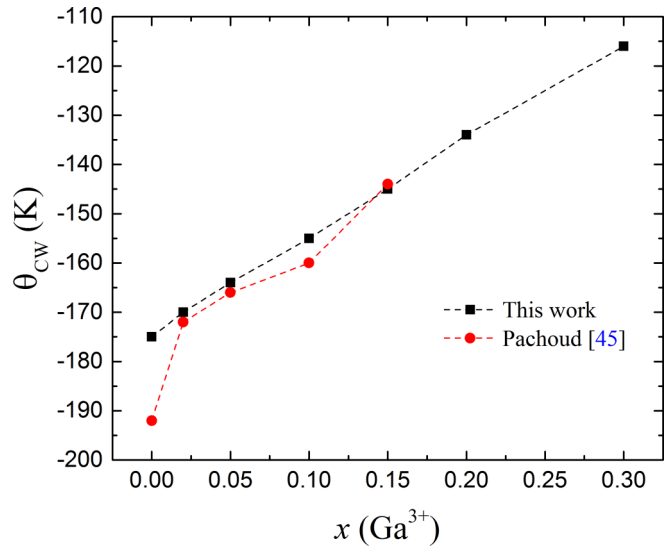


FIG. 14. Variation of the Curie-Weiss temperature versus x in $CuCr_{1-x}Ga_xO_2$.

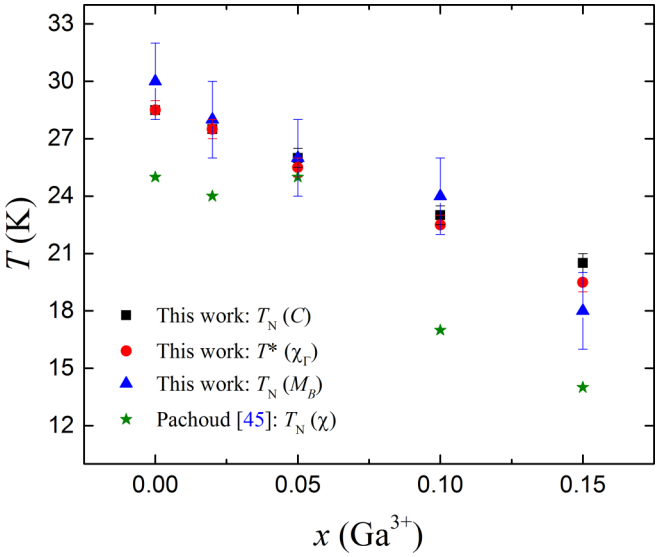


FIG. 15. Variation of the transition temperature as a function of x in $CuCr_{1-x}Ga_xO_2$.

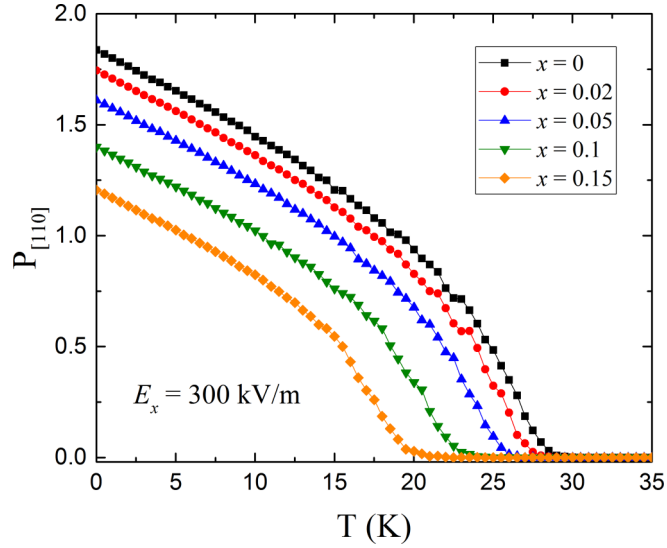


FIG. 16. Simulated temperature dependence of the ferroelectric polarization per magnetic bond along the [110] direction in $CuCr_{1-x}Ga_xO_2$.

out losing the antiferromagnetic nature of the system (Fig. 15). For $x \geqslant 0.2$, M_B continuously increases under the effect of B and does not show any clear anomaly at low temperatures, indicating that a phase transition to an antiferromagnetic state no longer exists. Such behavior is consistent with the loss of long-range ordering seen for $x \geqslant 0.2$ (Fig. 12). On the other hand, we find that Ga^{3+} doping enhances the frustration in the system where we see an increase in the frustration parameter $f = |\theta_{CW}|/T_N$ [61,62] with the increase of x, as shown in Table II. We thus meet the main two ingredients of spin glass systems [63]: frustration and disordered spins, and one can predict a spin-glass-like behavior for large Ga^{3+} fractions.

D. Ferroelectric properties

As shown in Sec. IV B, in the magnetically ordered states, $CuCr_{1-x}Ga_xO_2$ preserves its spiral ordering up to $x = 0.15$. Thus, the emergence of spontaneous ferroelectricity can still be described by the extended inverse DM model given by Eq. (1). Typically, we start our simulations from random spin configurations at $T_i = 35.01$ K, and we slowly cool the system down to $T_f = 0.01$ K with a constant temperature step $\Delta T = 0.5$ K. At each temperature and for the first 3×10^3 MC steps of the equilibration time, we apply a poling electric field $E_x = 300$ kV/m along the [110] direction to select a unique helicity for all atomic planes and thus a single ferroelectric domain as done experimentally. We then let the system relax to its equilibrium state during the remaining 2×10^3 MC steps at each temperature. Figure 16 shows the temperature profile of $P_{[110]}$ simulated for each fraction $x \leqslant 0.15$. It can be seen that $P_{[110]}$ decreases as x increases in the system. This decrease is caused by the loss of magnetic bonds and the destabilization of the ICY state. Also, it can be noticed that the temperature at which ferroelectricity starts to emerge decreases as x increases. This is because ferroelectricity is directly associated with spiral ordering in these compounds. We also simulate P-E hysteresis loops at $T = 5$ K for the various compositions (Fig. 17). For the pure system ($x = 0$), we find an electric coercive field $E_c \approx 53$ kV/m, in very good agreement with the one reported experimentally ($E_c = 51$ kV/m) [64]. Also, the saturation field $E_{sat} \approx 90$ kV/m shows a very

TABLE II. Estimated Néel and Curie-Weiss temperatures with their corresponding frustration parameter $f = |\theta_{CW}|/T_N$ obtained for $L = 147$ in $CuCr_{1-x}Ga_xO_2$.

	x				
	0	0.02	0.05	0.1	0.15
θ_{CW} (K)	−175	−170	−164	−155	−145
T_N (K)	28.0	26.5	25.0	21.5	18.0
f	6.25	6.42	6.56	7.21	8.06

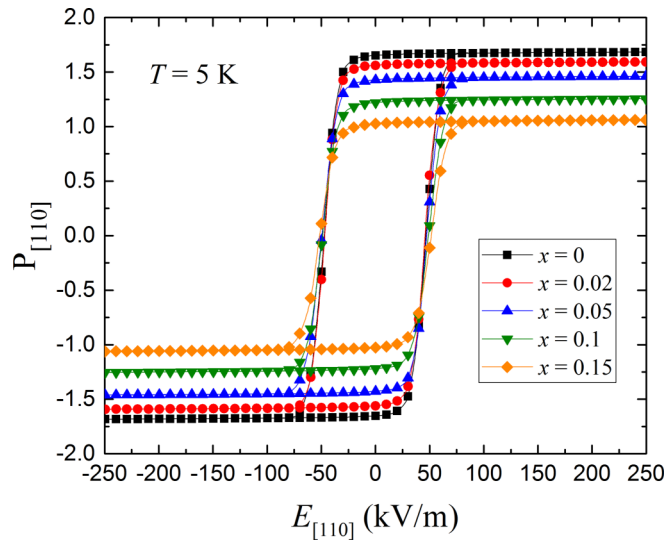


FIG. 17. P-E hysteresis loops simulated at $T = 5$ K in $CuCr_{1-x}Ga_xO_2$.

small dependence on the Ga fraction. Furthermore, we notice that the electric coercive field E_c remains roughly constant ($E_c \approx 53\,\mathrm{kV/m}$) for all fractions, which is a very important property in such multiferroics.

V. CONCLUSIONS

In this paper, the effects of Ga doping on magnetic and ferroelectric properties of multiferroic delafossite $CuCrO_2$ were investigated by means of DFT calculations and Monte Carlo simulations. DFT calculations showed that doping $CuCrO_2$ by Ga^{3+} in the Cr^{3+} sites does not significantly modify the present superexchange couplings. Monte Carlo simulations showed that Ga doping destabilizes the ICY state presented in $CuCrO_2$ even in the absence of applied fields. Our results suggested that $CuCr_{1-x}Ga_xO_2$ is still multiferroic for $x \leqslant 0.15$, while it became disordered at higher fractions. Up to this limit, the antiferromagnetic transition temperature is drastically affected by Ga doping while it is still accompanied by spiral ordering. Also we found that Ga impurities enhance the frustration in the system, leading to the possibility of a spin-glass-like behavior in $CuCr_{0.7}Ga_{0.3}O_2$. Finally, P-E hysteresis loops simulated in $CuCr_{1-x}Ga_xO_2$ showed a decrease in the saturation polarization caused by the introduced vacancies while preserving roughly the same electric coercive and saturation fields. Future investigations of this system and the effects of other types of dopants on the different properties of $CuCrO_2$ would be interesting. However, additional complications due to the risk of vacancy formation [65,66], for example, must be properly addressed.

ACKNOWLEDGMENTS

The authors acknowledge the financial support of the French Agence Nationale de la Recherche and LabEx EMC3 through the Project AFLTEPMAG (Grant No. ANR-10-LABX-09-01). Y.K. acknowledges the computational resources provided by the Swedish National Infrastructure for Computing (SNIC). The authors are also grateful to the Centre Régional Informatique et d'Applications Numériques de Normandie (CRIANN), where Monte Carlo simulations were performed as Project No. 2015004.

[1] R. D. Shannon, D. B. Rogers, and C. T. Prewitt, Inorg. Chem. **10**, 713 (1971).
[2] C. T. Prewitt, R. D. Shannon, and D. B. Rogers, Inorg. Chem. **10**, 719 (1971).
[3] D. B. Rogers, R. D. Shannon, C. T. Prewitt, and J. L. Gillson, Inorg. Chem. **10**, 723 (1971).
[4] M. A. Marquardt, N. A. Ashmore, and D. P. Cann, Thin Solid Films **496**, 146 (2006).
[5] R. Daou, R. Frésard, V. Eyert, S. Hébert, and A. Maignan, Sci. Technol. Adv. Mater. **18**, 919 (2017).
[6] H. Kawazoe, M. Yasukawa, H. Hyodo, M. Kurita, H. Yanagi, and H. Hosono, Nature (London) **389**, 939 (1997).
[7] T. Harada, K. Fujiwara, and A. Tsukazaki, APL Mater. **6**, 046107 (2018).
[8] H. Kuriyama, M. Nohara, T. Sasagawa, K. Takubo, T. Mizokawa, K. Kimura, and H. Takagi, in *Proceedings of the 25th International Conference on Thermoelectrics* (IEEE, Piscataway, NJ, 2006), p. 79.
[9] T. Nozaki, K. Hayashi, and T. Kajitani, J. Chem. Eng. Jpn. **40**, 1205 (2007).
[10] A. Maignan, V. Eyert, C. Martin, S. Kremer, R. Frésard, and D. Pelloquin, Phys. Rev. B **80**, 115103 (2009).
[11] E. Guilmeau, A. Maignan, and C. Martin, J. Electron. Mater. **38**, 1104 (2009).
[12] M. Mekata, N. Yaguchi, T. Takagi, S. Mitsuda, and H. Yoshizawa, J. Magn. Magn. Mater. **104**, 823 (1992).
[13] M. Mekata, N. Yaguchi, T. Takagi, T. Sugino, S. Mitsuda, H. Yoshizawa, N. Hosoito, and T. Shinjo, J. Phys. Soc. Jpn. **62**, 4474 (1993).
[14] O. A. Petrenko, G. Balakrishnan, M. R. Lees, D. McK. Paul, and A. Hoser, Phys. Rev. B **62**, 8983 (2000).
[15] T. Kimura, J. C. Lashley, and A. P. Ramirez, Phys. Rev. B **73**, 220401(R) (2006).
[16] F. Ye, Y. Ren, Q. Huang, J. A. Fernandez-Baca, P. Dai, J. W. Lynn, and T. Kimura, Phys. Rev. B **73**, 220404(R) (2006).
[17] V. Eyert, R. Frésard, and A. Maignan, Phys. Rev. B **78**, 052402 (2008).
[18] A. Maignan, C. Martin, R. Frésard, V. Eyert, E. Guilmeau, S. Hébert, M. Poienar, and D. Pelloquin, Solid State Commun. **149**, 962 (2009).
[19] X.-F. Jiang, X.-F. Liu, Y.-Z. Wu, and J.-R. Han, Chin. Phys. B **21**, 077502 (2012).
[20] S. Seki, Y. Onose, and Y. Tokura, Phys. Rev. Lett. **101**, 067204 (2008).
[21] K. Kimura, H. Nakamura, K. Ohgushi, and T. Kimura, Phys. Rev. B **78**, 140401(R) (2008).
[22] M. Soda, K. Kimura, T. Kimura, M. Matsuura, and K. Hirotam, J. Phys. Soc. Jpn. **78**, 124703 (2009).
[23] M. Soda, K. Kimura, T. Kimura, and K. Hirota, Phys. Rev. B **81**, 100406(R) (2010).
[24] H. Takatsu, S. Y. Onezawa, S. M. Ouri, S. Nakatsuji, K. T. Anaka, and Y. Maeno, J. Phys. Soc. Jpn. **76**, 104701 (2007).
[25] C. W. Hicks, A. S. Gibbs, A. P. Mackenzie, H. Takatsu, Y. Maeno, and E. A. Yelland, Phys. Rev. Lett. **109**, 116401 (2012).
[26] R. Daou, R. Frésard, S. Hébert, and A. Maignan, Phys. Rev. B **91**, 041113(R) (2015).
[27] V. Eyert, R. Frésard, and A. Maignan, Chem. Mater. **20**, 2370 (2008).
[28] In this compound the large anisotropy of the conductivity is understood to result from the large anisotropy of the Fermi velocity.
[29] A. Albaalbaky, Y. O. Kvashnin, D. Ledue, R. Patte, and R. Frésard, Phys. Rev. B **96**, 064431 (2017).
[30] M. Frontzek, J. T. Haraldsen, A. Podlesnyak, M. Matsuda, A. D. Christianson, R. S. Fishman, A. S. Sefat, Y. Qiu, J. R. D. Copley, S. Barilo, S. V. Shiryaev, and G. Ehlers, Phys. Rev. B **84**, 094448 (2011).
[31] J. P. Doumerc, A. Wichainchai, A. Ammar, M. Pouchard, and P. Hagenmuller, Mater. Res. Bull. **21**, 745 (1986).
[32] M. Poienar, F. Damay, C. Martin, V. Hardy, A. Maignan, and G. André, Phys. Rev. B **79**, 014412 (2009).

[33] K. Kimura, T. Otani, H. Nakamura, Y. Wakabayashi, and T. Kimura, J. Phys. Soc. Jpn. **78**, 113710 (2009).
[34] N. Terada, J. Phys.: Condens. Matter **26**, 453202 (2014).
[35] Y. Tokura and S. Seki, Adv. Mater. **22**, 1554 (2010).
[36] Y. Tokura, S. Seki, and N. Nagaosa, Rep. Prog. Phys. **77**, 076501 (2014).
[37] T. A. Kaplan and S. D. Mahanti, Phys. Rev. B **83**, 174432 (2011).
[38] T. Okuda, R. Kajimoto, M. Okawa, and T. Saitoh, Int. J. Mod. Phys. B **27**, 1330002 (2013).
[39] T. Okuda, K. Uto, S. Seki, Y. Onose, Y. Tokura, and R. Kajimoto, J. Phys. Soc. Jpn. **80**, 014711 (2011).
[40] F. Jlaiel, M. Amami, P. Strobel, and A. Ben Salah, Cent. Eur. J. Chem. **9**, 5 (2011).
[41] T. Okuda, Y. Beppu, Y. Fujii, T. Onoe, N. Terada, and S. Miyasaka, Phys. Rev. B **77**, 134423 (2008).
[42] T. Okuda, S. Oozono, T. Kihara, and M. Tokunaga, J. Phys. Soc. Jpn. **82**, 014706 (2013).
[43] M. Han, K. Jiang, J. Zhang, W. Yu, Y. Li, Z. Hu, and J. Chu, J. Mater. Chem. **22**, 18463 (2012).
[44] D. Xiong, Q. Zhang, S. K. Verma, H. Li, W. Chen, and X. Zhao, J. Alloys Compd. **662**, 374 (2016).
[45] E. Pachoud, K. Singh, Y. Bréard, C. Martin, G. André, V. Hardy, Ch. Simon, and A. Maignan, Phys. Rev. B **86**, 054437 (2012).
[46] T. Elkhouni, C. Colin, P. Strobel, A. Ben Salah, and M. Amami, J. Supercond. Novel Magn. **26**, 2125 (2013).
[47] M. T. Czyzyk and G. A. Sawatzky, Phys. Rev. B **49**, 14211 (1994).
[48] D. O. Scanlon, A. Walsh, B. J. Morgan, G. W. Watson, D. J. Payne, and R. G. Egdell, Phys. Rev. B **79**, 035101 (2009).
[49] J. M. Wills, O. Eriksson, M. Alouani, and D. L. Price, in *Electronic Structure and Physical Properties of Solids*, edited by H. Dreysse, Lecture Notes in Physics Vol. 535 (Springer, Berlin, 2000), pp. 148–167.
[50] G. Kresse and D. Joubert, Phys. Rev. B **59**, 1758 (1999).
[51] P. E. Blochl, Phys. Rev. B **50**, 17953 (1994).
[52] A. I. Liechtenstein, M. I. Katsnelson, V. P. Antropov, and V. A. Gubanov, J. Magn. Magn. Mater. **67**, 65 (1987).
[53] M. I. Katsnelson and A. I. Lichtenstein, Phys. Rev. B **61**, 8906 (2000).
[54] Y. O. Kvashnin, O. Grånäs, I. Di Marco, M. I. Katsnelson, A. I. Lichtenstein, and O. Eriksson, Phys. Rev. B **91**, 125133 (2015).
[55] D. P. Landau and K. Binder, *A Guide to Monte Carlo Simulations in Statistical Physics* (Cambridge University Press, Cambridge, 2008).
[56] N. Metropolis, A. W. Rosenbluth, M. N. Rosenbluth, A. H. Teller, and E. Teller, J. Chem. Phys. **21**, 1087 (1953).
[57] U. Nowak, R. W. Chantrell, and E. C. Kennedy, Phys. Rev. Lett. **84**, 163 (2000).
[58] F. A. Benko and F. P. Koffyberg, Mater. Res. Bull. **21**, 753 (1986).
[59] S. Zagoulaev and I. I. Tupitsyn, Phys. Rev. B **55**, 13528 (1997).
[60] D. Khomskii, Physics **2**, 20 (2009).
[61] A. P. Ramirez, Annu. Rev. Mater. Sci. **24**, 453 (1994).
[62] J. E. Greedan, J. Mater. Chem. **11**, 37 (2001).
[63] K. Binder and A. P. Young, Rev. Mod. Phys. **58**, 801 (1986).
[64] K. Kimura, H. Nakamura, S. Kimura, M. Hagiwara, and T. Kimura, Phys. Rev. Lett. **103**, 107201 (2009).
[65] H. Pan, J. B. Yi, L. Shen, R. Q. Wu, J. H. Yang, J. Y. Lin, Y. P. Feng, J. Ding, L. H. Van, and J. H. Yin, Phys. Rev. Lett. **99**, 127201 (2007).
[66] X. Wang, Y. Song, L. L. Tao, J. F. Feng, Y. Sui, J. Tang, B. Song, Y. Wang, Y. Wang, Y. Zhang, and X. F. Han, Appl. Phys. Lett. **105**, 262402 (2014).